Control of electro-optic sideband spectrum using sequential modulators

OPEN ACCESS
IOP Publishing
Journal of Optics
J. Opt. **27** (2025) 045803 (9pp)
https://doi.org/10.1088/2040-8986/adb860

Control of electro-optic sideband spectrum using sequential modulators

U Dammalapati*, R Elvin, P F Griffin and E Riis

SUPA, Department of Physics, University of Strathclyde, John Anderson Building, 107 Rottenrow East, Glasgow G4 0NG, United Kingdom

E-mail: umakanth.dammalapati@strath.ac.uk and e.riis@strath.ac.uk

Received 16 November 2024, revised 17 February 2025
Accepted for publication 20 February 2025
Published 4 March 2025

Abstract

Electro-optic modulators are widely used for the generation of optical sidebands for various applications. Here, we report on a technique enabling control of the relative amplitudes of optical sidebands generated by electro-optic modulators. The technique makes use of a phase modulator and Mach–Zehnder amplitude modulator, connected in series to break the symmetry of the sideband amplitudes. The generated optical sideband spectrum can be controlled by the two radio frequency (RF) modulation amplitudes, the attenuation level of the amplitude modulator, and the relative RF phase of the two modulations. We demonstrate near-complete suppression of one first-order sideband and with simultaneously achieving equal amplitudes of the carrier and the other first-order sideband with $>94\%$ purity. The technique can be utilised to produce a spectrum with effectively two frequency components. This enables application in atomic physics experiments such as the minimisation of off-resonant light shifts that can limit the performance of atomic clocks and interferometers. We demonstrate operation in the near-infrared, at 795 nm, using commercial-off-the-shelf components and circumventing the need for frequency doubling of lasers in the optical communications region.

Keywords: electro-optic modulator, phase modulator, Mach–Zehnder modulator, optical modulation

1. Introduction

Quantum technologies based on cold-atom systems are being explored extensively for miniaturisation to allow for field deployment of clocks [1] and quantum sensors [2, 3]; the latter with particular interest in atom interferometry [4] with applications such as in gravimetry [5]. In many of these experiments control of the frequency spectrum of the optical field is required for manipulation of the internal and external degrees of freedom of the atoms. One widely used method in cold-atom experiments is to make use of coherently driven two-photon Raman transitions. This technique has found applications in experiments related to atomic velocity selection [6], atom interferometry [7], and clocks based on coherent population trapping (CPT) [8–10]. These applications tend to employ addressing of atomic transitions in a Λ-configuration, connecting one excited state, typically with two ground state hyperfine levels. This optical configuration can be implemented through techniques such as optical phase-locking of two lasers [11, 12], injection locking of lasers [13, 14], direct modulation of the laser current [15], and a single laser with an electro-optic modulator (EOM), that produces two sidebands on either side of a carrier signal [16, 17]. The last method benefits from an inherent phase coherence and relative simplicity. However, in addition to the generation of optical sidebands that are required, other frequency components will also be present. In

* Author to whom any correspondence should be addressed.

precision experiments, this imposes a constraint as the additional frequencies can introduce additional undesirable interactions potentially affecting the measurement. For example, in atomic clock experiments, these spectral components lead to off-resonant light shifts [9, 18, 19] and additional phase shifts in atom interferometry experiments [20]. Furthermore, non-resonant frequency components do not contribute to the interrogation process and increase the total laser power, and hence also the noise, at the sample. These can be mitigated by generating only the required two frequency components having equal amplitudes.

Several methods have been developed and demonstrated for the generation of Raman beams containing only two frequencies using EOMs. Among the methods for achieving this are the combination of a phase modulator (PM) and a Fabry–Pérot etalon [21], a PM and a birefringent calcite crystal [22], and a PM and a fibre Bragg grating filter [23]; all of them use spectral filtering. The PM alone can be operated in the carrier suppressed mode, however, this happens at the expense of power in the second- and higher-order sidebands comparable to that in the first-order sidebands. Alternatively, a Mach–Zehnder intensity interferometer (MZM) can be run in a carrier suppressed mode while still creating equal amplitudes of the two first-order sidebands [24, 25]. Here, the amplitude of the sidebands depend on the strength of the modulation. Separate amplitude control of the frequency components can be achieved using a single-sideband modulation technique such as serrodyne modulation [26, 27], in-phase and quadrature (I/Q) modulation [4, 28, 29], and very recently silicon based MZM modulator (DP-MZM) [30]. Due to lack of availability of components, the latter two techniques can currently only be implemented in the optical communication region (C-band), and serrodyne modulation requires a high-fidelity sawtooth drive signal restricting maximum achievable frequency. Furthermore, generation of wavelengths around 760–780 nm from 1540–1560 nm range wavelength lasers works well for potassium (K) and rubidium (Rb) atoms, whereas for most other elements it does not. These techniques add complexity to the experimental setup, so alternative compact and reliable techniques are desirable for the applications mentioned above.

In this work we demonstrate a technique for obtaining controllable, in particular equal, amplitudes of carrier and one of the first-order sidebands while eliminating the other first-order sideband and limiting higher-order sidebands. Two EOMs are connected sequentially and driven by a single RF source, with an analogue phase shifter (PS) to control the relative phase of the modulations. One of the two EOMs functions as a PM and the other as a MZM. In this configuration, as the optical phase plays no role and therefore by optimising four parameters—the RF modulation amplitudes to the two EOMs, the relative RF phase, and the overall attenuation of the MZM—it is possible to widely control the relative amplitudes of the carrier and individual sidebands, including retaining the carrier and one sideband. Destructive interference of the modulations into the unwanted sideband is effective at suppressing this frequency component while $<6\%$ of the total output remains in the second-order sidebands.

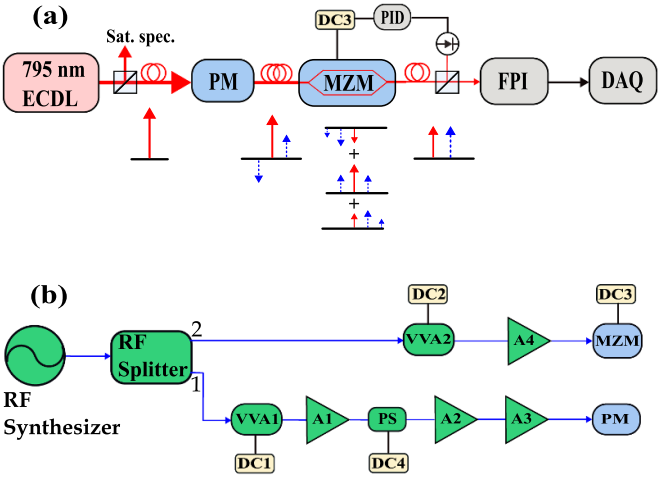

Figure 1. Experimental layout. (a) The optical layout and simplified principle of the technique is shown with carrier and first-order sidebands. Light from a 795 nm ECDL is coupled into the fibre pigtailed PM which is coupled into a fibre pigtailed MZM. The optical signals are measured with Fabry–Pérot interferometer and the signals are recorded on data acquisition system. The opposite optical phases imprinted on the first-order sidebands by the two modulators enable cancellation of one of them. (b) Radio frequency electronics. DC1-4: DC voltage supply; A1-4: RF amplifier; VVA1-2; Voltage Variable Attenuator; FPI: Fabry–Pérot interferometer; PM: Phase modulator; MZM: Mach–Zehnder modulator; PS: Phase shifter; PID: Proportional-Integral-Differential controller and DAQ: Data acquisition system.

2. Experimental setup

A schematic of the experimental setup is shown in figure 1 consisting of the optical layout along with the simplified principle of the technique (figure 1(a)) and the RF electronics employed for the reported measurements (figure 1(b)). The laser light is obtained from a commercial external cavity diode laser (ECDL) system (Moglabs, CEL) operating at a wavelength of 795 nm for Rb D_1 transition interrogation. It delivers a maximum output power of 100 mW. A small fraction of the optical power is used for saturated absorption spectroscopy for frequency stabilisation of the laser. For the presented measurements, about 1–2 mW is coupled into a commercial 10 GHz bandwidth polarisation maintaining pigtailed x-cut $LiNbO_3$ electro-optic PM (iXblue, NIR-MPX800-LN-10). The output from the PM is coupled into a MZM, which is also a commercial polarisation maintaining pigtailed x-cut $LiNbO_3$ EOM (iXblue, NIR-MX800-LN-10) with a 10 GHz modulation bandwidth. The MZM consists of a waveguide, which is

split into two arms where out-of-phase AC and DC modulation take place before recombination. The MZM has two control inputs; one for the RF voltage and the other for the DC bias voltage determining the overall modulator attenuation. The optical path difference between the two internal arms is adjusted by varying this DC bias voltage over ±20 V.

The output of the combined electro-optical system is monitored with a scanning Fabry–Pérot interferometer (FPI) (Thorlabs, SA200-8B) with a free spectral range (FSR) of 1.5 GHz and a finesse >200, which suffices for the present work. The measured transmission spectrum of the FPI (shown in figure 3(b)) is recorded on a computer with a data acquisition (DAQ) system. A fraction of the laser light after the MZM is split onto a low-bandwidth transimpedance photodiode amplifier (Thorlabs, PDA36A2, 12 MHz) and is used to stabilise the DC bias voltage of the MZM with a PID controller (Moku: GO) as described in section 4.3.

The RF source (figure 1(b)) consists of a highly stable RF synthesiser (Keysight E8257D) that delivers the desired RF signal with control over frequency and power. An RF splitter (Mini-Circuits, ZX10R-14-S+) divides an RF output power of -7 dBm into two arms: the PM arm and the MZM arm. The RF power supplied to each arm can be independently regulated by a voltage variable attenuator, VVA1 and VVA2 (Mini-Circuits, ZX73-123+). The PM arm also includes an analogue PS (Analog Devices; CMD297P34 evaluation board) that can be operated in the RF range 5–18 GHz. The phase shift is realised by applying DC voltage (DC4) varied from 0 to +10 V for a phase shift of 480 degrees. In the present configuration a total of three amplifiers are required in this arm, labelled A1, A2, and A3 in figure 1(b). A1 and A2 (Mini-Circuits, ZX60-83LN12+) account for the measured high insertion loss of the PS, while A3 (Mini-Circuits, ZVE-3 W-83+) provides the required output power. The MZM arm consists of a VVA2 and a high-gain amplifier, A4 (Mini-Circuits, ZVE-3 W-83+). Both modulators are characterised independently by measuring the distribution of power in the carrier and generated sidebands as a function of the applied RF power controlled by the VVAs. The RF voltage, $V_{\rm rms}$ in units of V_π, where, $\mathrm{V}_{rms} \propto \sqrt{P_{RF}}$ and $\mathrm{V}_\pi = V_{rms}\pi\sqrt{2}$ is used in the text.

3. Model

The combined effect of the PM and the amplitude modulator can be modeled analytically. First, we consider a PM driven by a harmonic signal with an angular RF frequency of Ω. We start with the familiar result that an input optical electric field $E(t) = E_0 \mathrm{e}^{-\mathrm{i}\omega t}$ of amplitude E_0 and angular frequency ω is transformed to an output field [31]:

$$E_{\rm out}(t) = E_0 \sum_{n=-\infty}^{\infty} J_n(\delta) \exp\left[-i(\omega + n\Omega)t\right] , \tag{1}$$

where $J_n(\delta)$ is the n^{th} order Bessel function and δ is the modulation index.

For the present model and experiment with a typical modulation index δ in the region of unity, it is adequate to treat this as the limit for $N \to \infty$ of the finite sum:

$$E_{\rm out}(t) = E_0 \sum_{n=-N}^{N} J_n(\delta) \exp\left[-i(\omega + n\Omega)t\right] . \tag{2}$$

This clearly demonstrates the spectrum of the light with carrier and sideband amplitudes determined by the Bessel functions evaluated for the relevant modulation index. Separating the terms out, we can represent each spectral component in the output by an entry in the following vector:

$$\begin{aligned} \mathrm{e}^{-\mathrm{i}\omega t} \{ & J_{-N}(\delta)\mathrm{e}^{\mathrm{i}N\Omega t}, \cdots, J_{-1}(\delta)\mathrm{e}^{\mathrm{i}\Omega t}, J_0(\delta), \\ & J_1(\delta)\mathrm{e}^{-\mathrm{i}\Omega t}, \cdots, J_N(\delta)\mathrm{e}^{-\mathrm{i}N\Omega t} \} . \end{aligned} \tag{3}$$

In general, and specifically for the second of the two cascaded modulators, the input field will already be a spectrum of sidebands separated by frequency Ω and each undergoing phase modulation. Hence, this input electric field can be represented in the same way as a vector with complex amplitudes $a_i,\ i \in \{-N, N\}$:

$$\vec{\nu}_{\rm in} = \mathrm{e}^{-\mathrm{i}\omega t} \left\{ a_{-N}\mathrm{e}^{\mathrm{i}N\Omega t}, \cdots, a_{-1}\mathrm{e}^{\mathrm{i}\Omega t}, a_0, a_1\mathrm{e}^{-\mathrm{i}\Omega t}, \cdots, a_N\mathrm{e}^{-\mathrm{i}N\Omega t} \right\} . \tag{4}$$

Each of these frequencies can be considered as a carrier for the EOM and have its own sidebands generated, which will add coherently. The effect of the EOM on this spectrum can therefore be determined by the following matrix multiplication:

$$\vec{\nu}_{\rm out} = M_{PM}(\delta, \theta) \cdot \vec{\nu}_{in} , \tag{5}$$

where $M_{PM}(\delta, \theta)$ is the $2N+1$ by $2N+1$ matrix:

$$\begin{pmatrix} J_0 & \cdots & J_{-N+1}\mathrm{e}^{\mathrm{i}(N-1)(\Omega t-\theta)} & J_{-N}\mathrm{e}^{\mathrm{i}N(\Omega t-\theta)} & J_{-N-1}\mathrm{e}^{\mathrm{i}(N+1)(\Omega t-\theta)} & \cdots & J_{-2N}\mathrm{e}^{\mathrm{i}2N(\Omega t-\theta)} \\ \vdots & \cdots & \vdots & \vdots & \vdots & \cdots & \vdots \\ J_{N-1}\mathrm{e}^{\mathrm{i}(1-N)(\Omega t-\theta)} & \cdots & J_0 & J_{-1}\mathrm{e}^{\mathrm{i}(\Omega t-\theta)} & J_{-2}\mathrm{e}^{\mathrm{i}2(\Omega t-\theta)} & \cdots & J_{-N-1}\mathrm{e}^{\mathrm{i}(N+1)(\Omega t-\theta)} \\ J_N\mathrm{e}^{-\mathrm{i}N(\Omega t-\theta)} & \cdots & J_1\mathrm{e}^{-\mathrm{i}(\Omega t-\theta)} & J_0 & J_{-1}\mathrm{e}^{\mathrm{i}(\Omega t-\theta)} & \cdots & J_{-N}\mathrm{e}^{\mathrm{i}N(\Omega t-\theta)} \\ J_{N+1}\mathrm{e}^{-\mathrm{i}(N+1)(\Omega t-\theta)} & \cdots & J_2\mathrm{e}^{-\mathrm{i}2(\Omega t-\theta)} & J_1\mathrm{e}^{-\mathrm{i}(\Omega t-\theta)} & J_0 & \cdots & J_{-N+1}\mathrm{e}^{\mathrm{i}(N-1)(\Omega t-\theta)} \\ \vdots & \cdots & \vdots & \vdots & \vdots & \cdots & \vdots \\ J_{2N}\mathrm{e}^{-\mathrm{i}2N(\Omega t-\theta)} & \cdots & J_{N+1}\mathrm{e}^{-\mathrm{i}(N+1)(\Omega t-\theta)} & J_N\mathrm{e}^{-\mathrm{i}N(\Omega t-\theta)} & J_{N-1}\mathrm{e}^{-\mathrm{i}(N-1)(\Omega t-\theta)} & \cdots & J_0 \end{pmatrix} \tag{6}$$

In equation (6), for simplicity, the arguments for the Bessel functions have been left out of the expression as they are all evaluated at the same modulation index, δ. The phase terms of $e^{-i\theta}$ are included here to account for the RF phase difference between the PM and the subsequent MZM.

The MZM is slightly more involved, due to the internal operation of the device. As already mentioned it consists of two arms each with AC and DC modulation, but with opposite signs of the modulations. Each AC part is represented by a PM matrix $M_{PM}(\pm\beta/\sqrt{2},0)$ as derived above, where β represents the MZM modulation index and $\sqrt{2}$ in the denominator takes into account the applied RF power split between the two arms. The DC part can be represented by the identity matrix I multiplied by a phase factor $\exp(\pm i\phi/2)$. Hence the overall transfer matrix of the MZM is:

$$M_{MZM}(\beta,\phi) = \left(M_{\mathrm{PM}}\left(\beta/\sqrt{2},0\right)\exp(i\phi/2) + M_{\mathrm{PM}}\left(-\beta/\sqrt{2},0\right)\exp(-i\phi/2)\right)/2\,. \quad (7)$$

The phase ϕ is directly controlling the optical phase in the device and hence the balancing of the MZM. Hence, in an experimental realisation of this scheme, any drifts over time in the interferometer will necessitate an active tracking of ϕ. The integrated nature of commercial waveguide devices and thermal stabilisation mitigate this problem. This is the only point where the setup is sensitive to the relative optical phase in the arms of the MZM.

The total effect of the two modulators can therefore be described by the matrix product

$$M_{\mathrm{Tot}} = M_{\mathrm{MZM}}(\beta,\phi)\cdot M_{\mathrm{PM}}(\delta,\theta)\,. \quad (8)$$

This is used as the basis for modeling the operation of the concatenated modulators with a single input frequency (carrier (C)), i.e. the only non-zero input amplitude is a_0.

The numerical model readily shows that the combination of the two modulators has a maximum effect on the output spectrum only at a value of $\theta = \pm\pi/2$. At this condition, either the left or right sideband destructively interferes if the modulation depths are chosen correctly with the two signs representing a respective output spectrum. Figure 2 illustrates the variation of the output spectrum as the MZM modulation index, β, is increased from 0 to 3 and with a PM modulation index $\delta = 1$, the MZM DC term set for 50% transmission ($\phi = \pi/2$) and the relative RF phase difference, θ, between the two modulators set at $\pi/2$. This modeling is done with a value of $N = 5$, which was found to be sufficient order for calculations. The linewidth of the spectral components shown in figure 2 is chosen arbitrarily to display the spectral features as they would appear experimentally on a spectrum analyser. In general, the suppression method will work for arbitrary sidebands and the amplitude of the second-order sidebands is set by the Bessel functions.

Figure 2 also demonstrates the spectral control afforded by the setup. Starting at the familiar output spectrum of a PM at $\beta = 0$ the addition of amplitude modulation results in destructive interference of the SB- sideband at the same time as the constructive interference on SB+. At $\beta = 0.9$, indicated by the black curve, the majority of the output power is evenly split between the carrier and the first upper sideband with remaining left in each of SB- and SB2+. Due to the DC phase control, half the power is lost in the MZM. Of the remaining output power, the model shows 46% in each of the indicated modes, carrier and SB+, and $<5\%$ in SB2+ and $<3\%$ in SB-. At a higher MZM modulation index, $\beta = 2$, the figure also demonstrates how SB+ becomes the dominant sideband with about 65% of the output power (red curve). The singular significant sideband SB+ in a band of $\pm 5\Omega$ makes this a potentially interesting basis for an agile frequency control scheme for an injection locked semiconductor laser [13].

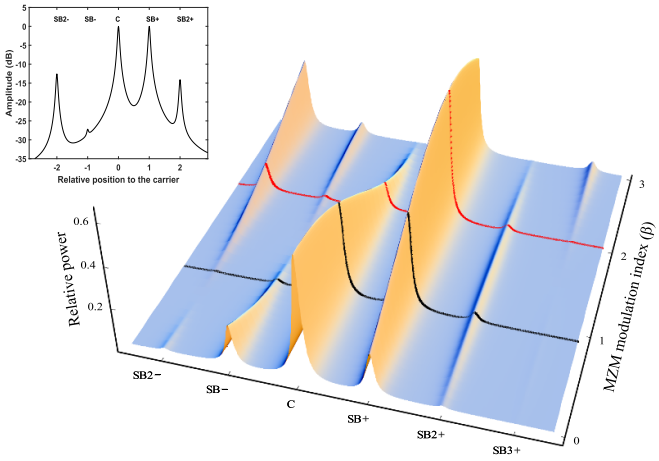

Figure 2. The numerically simulated amplitudes of the carrier (C), first-order sidebands (SB±) and higher-order sidebands (SB2±, SB3+), as a function of the MZM modulation index, β, at constant PM modulation index, $\delta = 1$, MZM DC bias control, $\phi = \pi/2$, and RF Phase difference between the two modulations, $\theta = \pi/2$. The black line shows the condition for $\beta = 0.9$, where the amplitudes of the carrier and plus first-order sideband are equal while SB- and second-order sidebands are suppressed. The red line corresponds to the maximised single sideband, SB+, at $\beta = 2$. *Inset*: The log-plot of the simulated optical spectrum of equal amplitudes of C and SB+ while SB- is suppressed for optimal values of $\delta = 0.87$, $\beta = 1.00$, $\phi = 1.68$, and $\theta = \pi/2$. The linewidth of the spectral components is chosen arbitrarily to display the spectral features.

The model allows for the optimisation of the four free parameters δ, β, ϕ and θ required for a given application and spectral requirement. Of particular interest for the intended application is equal power in the carrier and plus first-order sideband while minimising that of the adjacent SB- and SB2± sidebands. We empirically find that this is achieved for $\delta = 0.87$, $\beta = 1.00$, $\phi = 1.68$ and $\theta = \pi/2$ and the inset of figure 2 shows the corresponding log-plot of the spectrum demonstrating the parity of the powers of the two main modes (C and SB+) while demonstrating >25 dB reduction of the SB- and with suppressed higher modes. From the above optimum parameter values, a 10% variation of δ or a 20% variation of β keeping all other parameters constant changes the SB- amplitude by about a percent while still retaining the equal amplitudes of the carrier and SB+ with higher modes still suppressed.

Table 1. Experimental and model parameters.

Parameters	Experiment	Model
PM RF control (VVA1)	DC1	δ
MZM RF control (VVA2)	DC2	β
MZM DC bias voltage	DC3	ϕ
Phase shifter (PS)	DC4	θ

4. Results and discussion

The condition of equal amplitudes of the carrier and one first-order sideband while suppressing the other first-order sideband is demonstrated experimentally using four DC control parameters. They are PM RF amplitude through VVA1 (DC1), MZM RF amplitude through VVA2 (DC2), MZM DC bias voltage (DC3), and PS DC voltage (DC4). The experimental results are also numerically simulated with the model presented in section 3. The experimental parameters and their relation to the model parameters are given in table 1. The optimisation of the four experimental parameters and comparison of the experimental results with the model are discussed.

4.1. PS characterisation

The model presented in section 3 clearly demonstrates that the requirements for obtaining equal amplitudes of the carrier and one first-order sideband and to suppress the undesired first-order sideband is that a condition of $\pi/2$ phase between the two RF modulations must be met. This can be accomplished by adjusting the PS DC voltage (DC4). The voltage that fulfills this condition is determined iteratively; effectively, it is the unique voltage enabling carrier and one first-order sideband having equal amplitudes, while the other first-order sideband and the high-order sidebands are suppressed. Specifically, the amplitudes of the optical spectra of the carrier, first-order sidebands, and second-order sidebands are measured with the FPI at a fixed PS DC voltage by scanning the MZM DC bias voltage (DC3) at constant RF voltages to the PM ($V_{\mathrm{rms}}^{\mathrm{PM}}$) and MZM ($V_{\mathrm{rms}}^{\mathrm{MZM}}$). Confirmed by experiment, the model shows that this determination of the $\pi/2$ condition is insensitive to the chosen values of RF voltages. The method for further optimisation of these voltages is described in section 4.4. This is repeated for the PS DC voltage, scanning from 0 to 10 V in 1 V steps. From the optical spectra, the values of the MZM DC voltages corresponding to equal power in the carrier and one of the first-order sidebands and the power in all observed other sidebands relative to the total output are recorded. We observe that they exhibit a sinusoidal behaviour. As predicted by the model, these ratios vary with PS DC voltage, and $\pi/2$ is identified as a point where all sidebands apart from the desired one are minimised.

4.2. MZM DC bias voltage scan

The optical spectra of the carrier and sidebands are measured with the FPI at different DC bias voltages to the MZM at fixed RF voltages to the MZM ($V_{\mathrm{rms}}^{\mathrm{MZM}} = 0.22\,\mathrm{V}_\pi$) and PM ($V_{\mathrm{rms}}^{\mathrm{PM}} = 0.23\,\mathrm{V}_\pi$) and PS DC voltage corresponding to $\pi/2$ phase. Figure 3(a) shows the recorded spectral amplitudes of the carrier (C), plus first-order sideband (SB+), minus first-order sideband (SB-) and second-order sidebands (SB2+ and SB2-) as the MZM DC bias voltage (DC3) is varied from 0 V to 6 V in 0.2 V steps. The points are experimental data

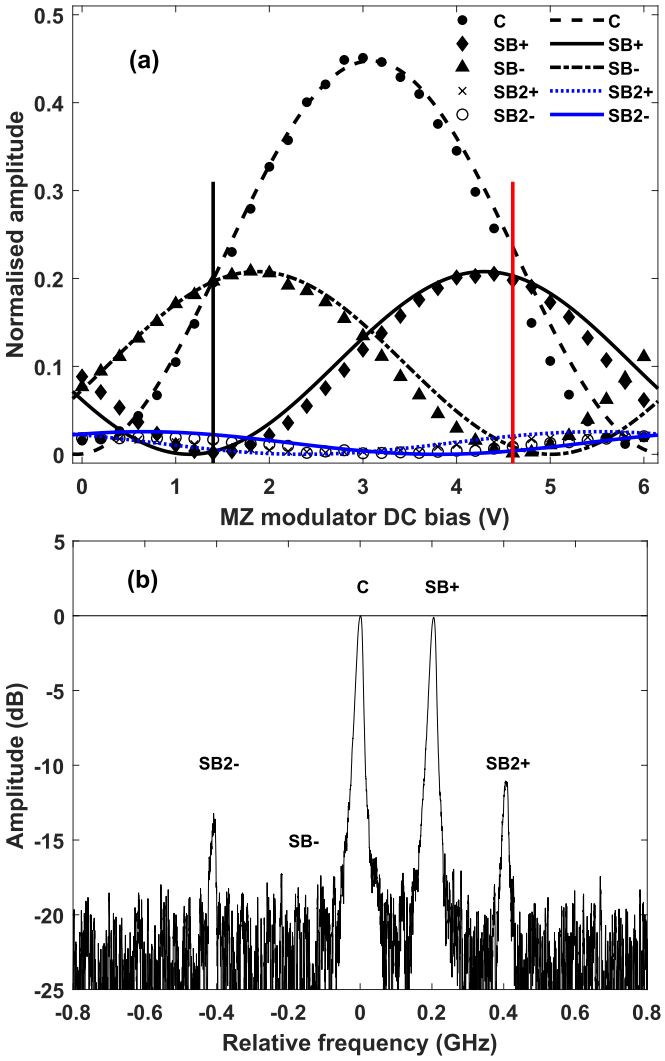

Figure 3. (a) The measured power of carrier (●), plus first-order sideband (SB+, ♦), minus first-order sideband (SB-, ▲), plus second-order sideband (SB2+, ×) and minus second-order sideband (SB2-, ○) are shown as a function of the MZM DC bias voltage for a PS DC voltage corresponding to phase $\theta = \pi/2$ and MZM and PM RF voltages kept constant, with the values indicated in the text. The red solid vertical line corresponds to the MZM DC voltage at which the measured carrier and plus sideband have equal amplitudes while the minus sideband is suppressed (b). The black vertical line corresponds to the DC voltage of MZM at which carrier and minus first-order sideband have equal amplitudes while the plus first-order sideband is suppressed. The curves (−−,−·,− in black and ··,− in blue) are the numerical calculations from the model presented in section 3. (b) The FPI spectrum of suppressed minus first-order sideband. The experimental data shown are a fifteen-point moving average. Here the laser frequency is fixed and the RF frequency of 6.2 GHz is chosen such that the sidebands appear at ±0.2 GHz (SB±) and ±0.4 GHz (SB2±) relative to the carrier due to the ∼1.5 GHz FSR of the FPI.

and the curves are from the numerical model described in section 3. For simplicity, the corresponding FPI spectra are fitted with a sum of Lorentzian functions and the respective amplitudes and peak positions of the carrier and sidebands are determined. In this work for ease of display, the FPI results presented were measured at an RF frequency of 6.2 GHz due to the 1.5 GHz FSR of the scanning FPI. Both modulators are wideband, 0–10 GHz, and as such can be readily tuned to the hyperfine ground state splitting of all the (stable) alkali elements.

The ability to suppress one first-order sideband while achieving equal amplitudes of the carrier and the other first-order sideband is demonstrated in figure 3(a). The solid red vertical line indicates the DC bias voltage of the MZM where the measured amplitudes of the carrier and plus first-order sideband are equal, the amplitude of the minus first-order sideband is suppressed, as well as the minimal amplitudes of the second order sidebands. The corresponding FPI spectrum is shown in figure 3(b). The slight deviation in position of the sidebands is attributed to the non-linearity of the piezo scan of the FPI. It can be observed that the amplitude of the minus first-order sideband is suppressed by $\geqslant$20 dB with respect to the amplitudes of the carrier and plus first-order sideband. The amplitudes of the second-order sidebands are about 12 dB lower than the carrier and plus first-order sideband while the 3rd and high-order sidebands are below the noise level. Comparing our results to various methods reported in the literature, serrodyne modulation at 850 nm reported up to 17 dB suppression of higher-order sidebands, which is limited to RF frequencies around 1 GHz [26], whereas the presented measurements were performed at 6.2 GHz at 795 nm. In the case of I/Q modulators, operated in the optical communication region, which is frequency doubled to 780 nm, work [4] has achieved more than 20 dB suppression and discussed the implications of the higher-order modes in the Raman atom beam splitting. Up to 18.4 dB suppression was achieved in [23] and in [30] the authors reported more than 30 dB on higher order suppression. This might be due to the non-linear interaction process and mature technology at optical communication wavelengths [32].

The curves shown in figure 3(a) are numerically simulated with the model presented in section 3. The four parameters values are $\delta = 1.02, (V_{\mathrm{rms}}^{\mathrm{PM}} = 0.23\,\mathrm{V}_{\pi})$, $\theta = \pi/2$, $\beta = 0.98, (V_{\mathrm{rms}}^{\mathrm{MZM}} = 0.22\,\mathrm{V}_{\pi})$, and ϕ varied from 0 to 3π. The experimental results of suppression of the minus first-order sideband to the noise level and 12 dB suppression of the second-order sidebands are in good agreement with the model estimations, where about 5% of the second-order sidebands remain while the minus first-order sideband is completely suppressed as shown in figure 3(a). The deviation of the experimental data from the model spectra is about 15% and is due to the non-linearities and imperfections of the MZM device [33].

Similarly, in figure 3(a), the black vertical line represents the MZM DC bias voltage at which amplitude of the plus first-order sideband is suppressed, equal amplitudes of carrier and minus first-order sideband and small amplitude of the second-order sidebands. In figure 3(a), the results are normalised to the maximum possible optical output power, when the MZM is fully on with the RF not applied, i.e. ϕ tuned to the maximum output, thus normalising out coupling losses.

4.3. MZM DC bias stabilisation

One of the known issues with an MZM is the 'bias drift' phenomenon [33, 34]. The device is fundamentally an optical interferometer and therefore sensitive to sub-wavelength-scale changes in the optical path length difference within the device MZM. Hence, a drift of the transfer function with time is expected due to environmental effects and requires compensation by adjusting the MZM DC bias voltage to maintain the desired position. Various methods have been used to circumvent this drift [35–38]. For I/Q modulators at optical communication wavelengths and MZMs in the near-infrared wavelengths, DC bias voltage controllers are commercially available. Depending on the application, the MZM DC bias voltage is stabilised either to the maximum or minimum or to the positive/negative quadrature (linear part) of the output transfer function. An integrated solution has been implemented for I/Q modulators, which have an internal monitor photodiode [4]. Furthermore, an analog stabilisation method for an I/Q modulator was demonstrated, where an auxiliary modulation tone was used to generate an error signal [39].

For the device used in this work there is no internal monitor photodiode, so the time averaged optical output power is recorded with a photodiode at the output of the MZM and is fed to a PID controller having proportional gain 14.9 dB and integrator bandwidth 10 Hz that regulates the MZM DC bias voltage (DC3) to the quadrature of the MZM transfer function. The stability of the optical power is observed to maintain the equal amplitudes of the carrier and one first-order sideband, here, SB+, that correspond to the quadrature of the MZM transfer function (solid red line in figure 3(a)). Hence, the corresponding photodiode signal is used directly compared to a setpoint to generate the error signal for controlling the bias voltage resulting in the equal amplitudes as shown in figure 3(b). The stability of the lock is within 1% of the set value and was checked for more than two hours for the work shown here. In addition, the MZM is enclosed in 1 cm thick foam, isolating it from ambient temperature variations. Similarly, the equal amplitudes of the carrier and SB- (solid black line in figure 3(a)) on the MZM transfer function correspond to a different MZM DC bias voltage. The results shown in figures 4 and 5 were taken stabilising the MZM DC bias voltage.

4.4. RF voltages optimisation

This work aims to demonstrate operating conditions for 1:1 operation of an RF carrier with a single first-order sideband, with elimination of the other, undesired first-order sideband. In figure 4, we demonstrate how these two conditions can be reconciled by an appropriate choice of RF voltages to the two EOMs. Figure 4(a) shows the minus first-order sideband amplitudes as a function of PM RF voltage for four different MZM RF voltages. The experimental data are fitted with a quadratic function to determine the PM RF voltage yielding the minimum value of this unwanted sideband and show

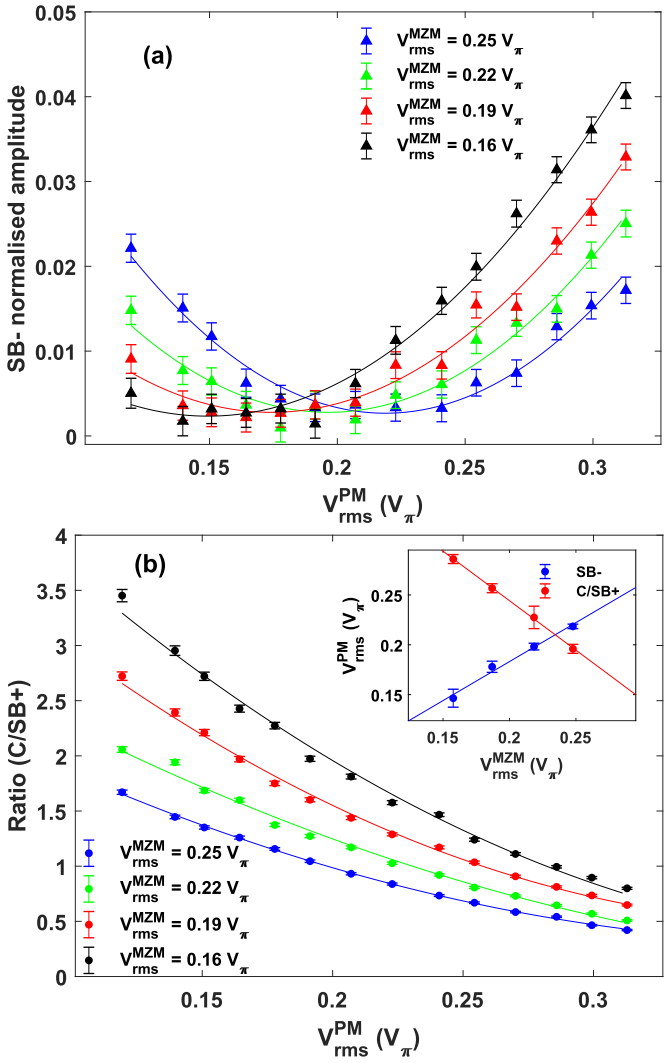

Figure 4. (a) Amplitudes of minus first-order sideband as a function of PM RF voltage ($V_{\rm rms}^{\rm PM}$) at four values of MZM RF voltages ($V_{\rm rms}^{\rm MZM}$). (b) The carrier to plus first-order sideband ratios vs. the PM RF voltage at four MZM RF voltage values. Both sets of data are observed to closely follow quadratic functions. For each MZM RF voltage fits to these are used to determine the minimum value of the minus first-order sideband as well as the PM RF voltage yielding a unity ratio of the carrier and plus first-order sideband. The errors quoted are one standard deviation for the experimental data. For all the measurements, the PS DC voltage corresponds to a phase of $\theta = \pi/2$, and the MZM DC bias voltage is stabilised using the PID controller. *Inset*: The PM RF voltage ($V_{\rm rms}^{\rm PM}$) vs. MZM RF voltage ($V_{\rm rms}^{\rm MZM}$) for minus first-order sideband (SB-, blue) and for unity carrier to plus first-order sideband ratio (C/SB+, red).

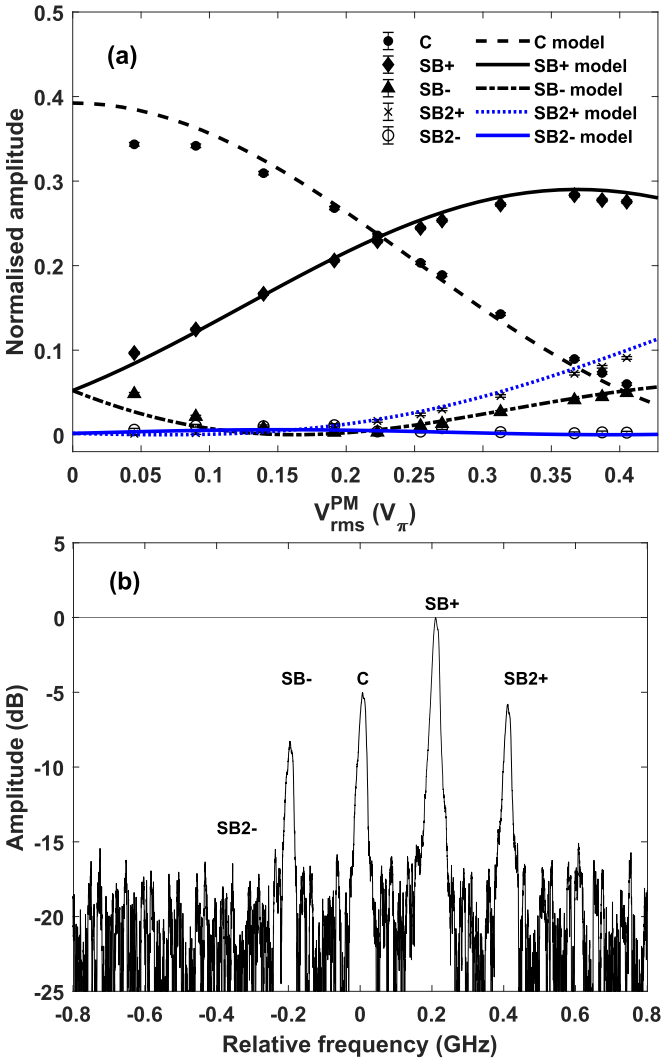

Figure 5. (a) The measured amplitudes of carrier, first-order, and second-order sidebands as a function of the variation of PM RF voltage for a fixed MZM RF voltage ($V_{\rm rms}^{\rm MZM} = 0.22\,{\rm V}_\pi$), MZM DC bias voltage (V), and PS voltage corresponding to phase $\pi/2$. The y-axis is normalised to the input optical power. The curves ($--,-,-\cdot$ in black and $\cdot\cdot,-$ in blue) are the numerical calculations from the model in section 3. The model parameters are: $\theta = \pi/2$, $\beta = 0.98$, ($V_{\rm rms}^{\rm MZM} = 0.22\,{\rm V}_\pi$), $\phi = \pi/2$ and δ varied from 0 to 2, ($V_{\rm rms}^{\rm PM} = 0.45\,{\rm V}_\pi$). (b) The full spectrum with the value corresponding to the PM RF voltage, $V_{\rm rms}^{\rm PM} = 0.36\,{\rm V}_\pi$ where SB+ is maximum.

a clear increase in this optimal PM RF voltage with increasing MZM RF voltage. This agrees with the numerical calculations indicating that both PM and MZM could be operated at relatively low RF voltages while rejecting the unwanted sideband efficiently. Figure 4(b) shows for the same parameters the ratio of the carrier to plus first-order sideband (C/SB+) as a function of PM RF voltage. The experimental values are fitted again with a quadratic function and show clearly that the unity value of the C/SB+ ratio is obtained for a lower PM RF voltage as the MZM RF voltage is increased. The inset of figure 4(b) demonstrates this opposite behaviour of the two criteria and identifies the cross-over where the MZM and the PM RF voltages can be tuned to satisfy both criteria.

The variation of the spectral components with increasing PM RF voltage is shown in figure 5(a) for a constant MZM RF voltage, MZM DC bias voltage, and PS voltage corresponding to phase $\pi/2$, respectively. Here, the PM RF voltage is varied in steps of $\sim 0.04\,{\rm V}_\pi$ from 0 to $0.41\,{\rm V}_\pi$, approximately equal to 1.82 V. At low RF voltage, nearly 80% of the power is in the carrier, and the remaining 20% is distributed among the sidebands. With increasing RF voltage, a condition is reached at which the carrier and SB+ have equal amplitudes while the

SB- is suppressed along with the second-order sidebands. With further increase of the RF voltage, the carrier is minimised, and second-order sideband starts to increase in addition to the first-order sidebands. It illustrates the parameters needed for obtaining the suppression of SB- and higher-order sidebands. The curves shown in figure 5(a) are based on the numerical model presented in section 3 and are in good agreement with the experimental results. The experimental data are normalised to the input optical power corrected for insertion losses in order to compare with the model. The observed $<10\%$ difference between the experimental values and the numerical calculations is attributed to deviations from ideal EOM performance and variation of other experimental parameters.

Furthermore, it is apparent that at RF voltages around $V_{\mathrm{rms}}^{\mathrm{PM}} = 0.36\,\mathrm{V}_{\pi}$, $\sim 60\%$ of the total output power goes into the plus first-order sideband. The carrier and plus second-order sideband share about 14% each, whereas the remaining power goes into the minus first-order sideband while the minus second-order sideband is suppressed and the 3rd and higher-order sidebands are below the noise level. The FPI spectrum corresponding to the above condition is shown in figure 5(b). For single-sideband operation, the model estimates that for the parameters $\delta = 1.3, (V_{\mathrm{rms}}^{\mathrm{PM}} = 0.3\,\mathrm{V}_{\pi})$, $\beta = 1.8, (V_{\mathrm{rms}}^{\mathrm{MZM}} = 0.4\,\mathrm{V}_{\pi})$, $\theta = \pi/2$, and $\phi = \pi/2$, up to 69% of the output power can be obtained into a single sideband, here, SB+ with about 10% each in the carrier, SB2±, and $<1\%$ in SB-. We note that greater spectral suppression in the range $\pm 2\Omega$ is observed for $\beta = 3$, at the cost of a reduction in the total power in the desired sideband as shown in figure 2.

5. Conclusion and outlook

In conclusion, we have demonstrated a technique for controlling the optical sideband spectrum based on sequential EOMs at near-infrared wavelengths. A phase and an amplitude modulator were driven by the same RF frequency and with an adjustable phase difference. It realises the suppression of one of the first-order sidebands while achieving equal power in the carrier and the other first-order sideband and less than 6% in higher-order sidebands. The method is implemented with commercial fibre-coupled modulators with 10 GHz bandwidth. It is readily applicable to many atomic physics experiments where Raman beams are required, such as atomic clocks and atom interferometers, bypassing the need for C-band components. In the near future, this technique will be implemented to demonstrate the mitigation of light shifts due to off-resonance light and for the determination of the frequency stability of a ^{87}Rb microwave CPT clock using ultra-cold atoms produced in a compact grating magneto-optical trap [40, 41]. We note that a similar arrangement of cascaded amplitude and PMs was previously used to minimise chromatic dispersion effects in fibre links [42].

As described, our method uses a PM and a MZM modulator in series. In the I/Q modulator, two MZM modulators effectively are used in parallel. However, in that case there are three optical phases that need to be stabilised, whereas the present setup only has one controlled by the MZM DC bias voltage, which can be servoed to an averaged output power. The approximately 5 dB optical insertion loss of each modulator and their maximum optical power rating limit the available output power to the few mW range. However, there is a clear way forward to eliminate one modulator that simplifies the RF electronics significantly. As explained above, the MZM consists of two arms where the same RF modulation is applied with opposite phases. If each of these arms were independently electrically accessible, the RF modulation currently applied to the PM could be added to the two arms. This configuration would require the same RF setup used in the present demonstration: the two controllable RF voltages with variable phase difference would be applied to independently accessed arms of a MZM. Furthermore, the remaining second-order light is primarily due to the second orders of the PM, i.e. for a PM only situation, there are equal plus and minus second sidebands. The beat between these and carrier will therefore add in phase and to lower order cancel the beat between the plus and minus firs-order sideband. It is possible to suppress the second-order sidebands by adding in some amplitude modulation at twice the normal modulation frequency at right RF phase. However, this could not be implemented in the present work as that is outside the bandwidth of the modulators and it would be interesting to investigate with advanced modulation schemes.

As shown in the data (figure 5) and further supported by the model, the sequential modulators also offer the possibility of transferring the majority of the optical power into a single sideband. This could be used either as is or for injecting into another laser [43]. The latter would not only increase the power level but also clean up the spectral properties of the amplified output. This has a clear advantage at GHz-level modulation frequencies over the demonstrated serrodyne technique [26, 27], which relies on a sawtooth RF signal, i.e. one with very high harmonic content.

Data availability statement

All data underpinning this publication are openly available from the University of Strathclyde KnowledgeBase at https://doi.org/10.15129/613fa5fb-54a5-48c9-b249-81045dc2f92f [44].

Acknowledgments

The work has been supported by the UK Engineering and Physical Sciences Research Council under Grant No. EP/T001046/1. The authors acknowledge Aidan Arnold, James McGilligan and Jonathan Pritchard for helpful discussions.

Conflict of interest

The authors declare no conflicts of interest.

ORCID iDs

U Dammalapati https://orcid.org/0000-0002-7086-036X
R Elvin https://orcid.org/0000-0003-0450-4727
P F Griffin https://orcid.org/0000-0002-0134-7554
E Riis https://orcid.org/0000-0002-3225-5302

References

[1] Ludlow A D, Boyd M M, Ye J, Peik E and Schmidt P O 2015 *Rev. Mod. Phys.* **87** 637
[2] Degen C L, Reinhard F and Cappellaro P 2017 *Rev. Mod. Phys.* **89** 035002
[3] Bongs K, Bennett S and Lohmann A 2023 *Nature* **617** 672–5
[4] Templier S, Hauden J, Cheiney P, Napolitano F, Porte H, Bouyer P, Barrett B and Battelier B 2021 *Phys. Rev. Appl.* **16** 044018
[5] Bidel Y, Carraz O, Charrière R, Cadoret M, Zahzam N and Bresson A 2013 *Appl. Phys. Lett.* **102** 144107
[6] Kasevich M, Weiss D S, Riis E, Moler K, Kasapi S and Chu S 1991 *Phys. Rev. Lett.* **66** 2297–300
[7] Kasevich M and Chu S 1991 *Phys. Rev. Lett.* **67** 181–4
[8] Wynands R and Nagel A 1999 *Appl. Phys.* B **68** 1–25
[9] Esnault F X, Blanshan E, Ivanov E N, Scholten R E, Kitching J and Donley E A 2013 *Phys. Rev.* A **88** 042120
[10] Elvin R, Hoth G W, Wright M, Lewis B, McGilligan J P, Arnold A S, Griffin P F and Riis E 2019 *Opt. Exp.* **27** 38359–66
[11] Santarelli G, Clairon A, Lea S and Tino G 1994 *Opt. Commun.* **104** 339–44
[12] Olivares-Rentería G, Lancheros-Naranjo D, Gomez E and Franco-Villafañe J 2020 *Phys. Rev.* A **101** 043613
[13] Kobayashi S and Kimura T 1981 *IEEE J. Quantum Electron.* **17** 681–9
[14] Liu Z and Slavík R 2020 *J. Lightwave Technol.* **38** 43–59
[15] Kitching J, Knappe S, Vukicevic M, Hollberg L, Wynands R and Weidmann W 2000 *IEEE Trans. Instrum. Meas.* **49** 1313–7
[16] Lee P, Blinov B, Brickman K, Deslauriers L, Madsen M, Miller R, Moehring D, Stick D and Monroe C 2003 *Opt. Lett.* **28** 1582–4
[17] Dotsenko I, Alt W, Kuhr S, Schrader D, Müller M, Miroshnychenko Y, Gomer V, Rauschenbeutel A and Meschede D 2004 *Appl. Phys.* B **78** 711–7
[18] Blanshan E, Rochester S M, Donley E A and Kitching J 2015 *Phys. Rev.* A **91** 041401
[19] Pollock J W, Yudin V I, Shuker M, Basalaev M Y, Taichenachev A V, Liu X, Kitching J and Donley E A 2018 *Phys. Rev.* A **98** 053424
[20] Carraz O, Charrière R, Cadoret M, Zahzam N, Bidel Y and Bresson A 2012 *Phys. Rev.* A **86** 033605
[21] Lee K S, Kim J, Lee S B, Park S E and Kwon T Y 2015 *J. Korean Phys. Soc.* **67** 318–22
[22] Arias N, Abediyeh V, Hamzeloui S and Gomez E 2017 *Opt. Exp.* **25** 5290–301
[23] Macrae C D, Bongs K and Holynski M 2021 *Opt. Lett.* **46** 1257–60
[24] Cooper N, Bateman J, Dunning A and Freegarde T 2012 *J. Opt. Soc. Am.* B **29** 646–9
[25] Liu X, Mérolla J M, Guérandel S, Gorecki C, de Clercq E and Boudot R 2013 *Phys. Rev.* A **87** 013416
[26] Houtz R, Chan C and Müller H 2009 *Opt. Exp.* **17** 19235
[27] Johnson D, Hogan J, Chiow S W and Kasevich M 2010 *Opt. Lett.* **35** 745–7
[28] Izutsu M, Shikama S and Sueta T 1981 *IEEE J. Quantum Electron.* **17** 2225–7
[29] Zhu L, Lien Y H, Hinton A, Niggebaum A, Rammeloo C, Bongs K and Holynski M 2018 *Opt. Exp.* **26** 6542–53
[30] Kodigala A *et al* 2022 arXiv: 2204.12537
[31] Yariv A 1989 *Quantum Electronics* (Wiley)
[32] Wooten E *et al* 2000 *IEEE J. Sel. Top. Quantum Electron.* **6** 69–82
[33] Salvestrini J P, Guilbert L, Fontana M, Abarkan M and Gille S 2011 *J. Lightwave Technol.* **29** 1522–34
[34] Nagata H, Kiuchi K and Saito T 1994 *J. Appl. Phys.* **75** 4762–4
[35] Bui D T, Nguyen C T, Ledoux-Rak I, Zyss J and Journet B 2011 *Meas. Sci. Technol.* **22** 125105
[36] Fu Y, Zhang X, Hraimel B, Liu T and Shen D 2013 *IEEE Microw. Mag.* **14** 102–7
[37] Švarnỳ J 2010 Analysis of quadrature bias-point drift of Mach-Zehnder electro-optic modulator *2010 12th Biennial Baltic Electronics Conf.* (IEEE) pp 231–4
[38] Fabbri S, O'Riordan C, Sygletos S and Ellis A 2013 *Electron. Lett.* **49** 135–6
[39] Wald S, Diorico F and Hosten O 2023 *Appl. Opt.* **62** 1–7
[40] Nshii C C, Vangeleyn M, Cotter J P, Griffin P F, Hinds E, Ironside C N, See P, Sinclair A, Riis E and Arnold A S 2013 *Nat. Nanotechnol.* **8** 321–4
[41] McGilligan J P, Griffin P F, Elvin R, Ingleby S J, Riis E and Arnold A S 2017 *Sci. Rep.* **7** 384
[42] Davies B and Conradi J 1998 *IEEE Photon. Technol. Lett.* **10** 600–2
[43] Agnew N, Lowit D and Arnold A S 2024 arXiv:2404.16806 [physics.atom-ph]
[44] (Available at : https://doi.org/10.15129/613fa5fb-54a5-48c9-b249-81045dc2f92f)